BUTTERWORTH HEINEMANN

Kinematics of the quasi-coherent vortical structure in near-wall turbulence

Nobuhide Kasagi, Yasushi Sumitani, Yuji Suzuki, and Oaki Iida
Department of Mechanical Engineering, The University of Tokyo, Bunkyo-ku, Tokyo, Japan

Near-wall turbulence structures in a direct numerical simulation database of turbulent channel flow were investigated by using a three-dimensional (3-D) computer graphics software tool. Several candidate methods to detect near-wall vortical structures were tested. They were based on instantaneous flow properties such as pressure, vorticity, enstrophy, dissipation rate, and the second invariant of deformation tensor. Among them, the low-pressure regions and those of negative second invariant of the deformation tensor corresponded well to the cores of vortical fluid motion. The spatial distribution of each term in the Reynolds stress transport equations was also examined in the instantaneous field to explore the role of vortical structures in production and destruction of the Reynolds stresses. It is found that these terms are distributed highly intermittently in space; intense production occurs mostly on both sides of near-wall streamwise vortices, and high redistribution, diffusion, and destruction regions also exist near around the vortices. High helicity regions are found to be associated with the elongated near-wall streaky structures.

Keywords: turbulence; wall turbulence; direct numerical simulation; coherent structure; streamwise vortex; visualization; Reynolds stress; channel flow; helicity

Introduction

Because the near-wall region is crucial for momentum, heat and mass transfer, understanding its structure and associated transport mechanism is of great importance from both scientific and engineering viewpoints. The pioneering work made by Stanford researchers, such as Kline et al. (1967) and Kim et al. (1971), revealed that the near-wall region of turbulent boundary layer exhibits recognizable streaky structures that are fairly periodic in the spanwise direction. They also documented deterministic behavior of a fluid motion producing the Reynolds stresses, which is labeled as bursting. Since then, a number of studies, based mainly on experimental techniques and sophisticated data processing, have been made to deepen our physical understanding of near-wall turbulence (see, e.g., Cantwell 1981; Robinson 1991a). However, owing to limited information obtained from the experimental measurements, the spatial relationship between various structures found as well as their underlying dynamics still remain unknown.

With the recent advances in large-scale computers, direct numerical simulation (DNS) has become a valuable resource for turbulence research. Unlike laboratory experiments, DNS provides such valuable information as velocity, pressure, and vorticity at any point and time in the turbulent flow field. Robinson et al. (1990) was the first to apply a three-dimensional (3-D) computer graphics technique to an investigation of turbulent structures in a DNS database. They identified the various structures experimentally observed, such as low- and high-speed streaks, arch-like vortical structures, and local high-shear layers, in the turbulent boundary layer numerically simulated by Spalart (1988). They also found that the marked vortical structures, of which cores were identified as local low-pressure regions, are in close spatial association with the two major modes of turbulent motion generating the Reynolds shear stress; i.e., ejections and sweeps. Lyons et al. (1989) found in their channel flow DNS database that quadrant two (ejection) and quadrant four (sweep) events, which possess a streaky structure, are associated with closed roller eddies in the cross-stream plane and that these eddies, on average, have a spanwise dimension of 50 wall units and a streamwise dimension of 400 ~ 450 wall units.

In the present study, near-wall turbulence structures in a DNS database of turbulent channel flow were visualized and examined by using a 3-D computer graphics software tool. The goal of this study is to reveal the detailed kinematics and associated turbulence mechanisms of the quasi-coherent vortical structures near the wall. The knowledge thus obtained should be useful for advancing our basic understanding of the physics of turbulence, and hence, certainly crucial for developing and improving closure models and control methodologies of turbulent transport phenomena.

Direct numerical simulation database and visualization technique

Features of the DNS database of a fully developed turbulent channel flow (Kuroda et al. 1994) used in the present study are summarized as follows. The Reynolds number based on the friction velocity u_τ and the channel half-width δ is 150. The computation was executed on $128 \times 97 \times 128$ grid points in the streamwise x, wall-normal y, and spanwise z directions, respectively. The computational domain was $5\pi\delta \times 2\delta \times 2\pi\delta$ in the x-, y- and z-directions, respectively. A spectral method; i.e., Fourier series in the x- and z-directions and a Chebyshev polynomial expansion in the y-direction, were employed. Accuracy and reliability of this DNS database have been confirmed to be sufficient through extensive comparison of the calculated turbulent statistics and instantaneous flow patterns

Address reprint requests to Professor N. Kasagi, Department of Mechanical Engineering, The University of Tokyo, 7-3-1, Bunkyo-ku, Tokyo 113, Japan. Telephone: 03-3812-2111, Telefax: 03-5800-6999, E-mail: kasagi@thtlab.t.u-tokyo.ac.jp.

Received 26 April 1994; accepted 25 August 1994

Int. J. Heat and Fluid Flow 16: 2–10, 1995

655 Avenue of the Americas, New York, NY 10010

0142-727X/95/$10.00
SSDI 0142-727X(94)00006-X

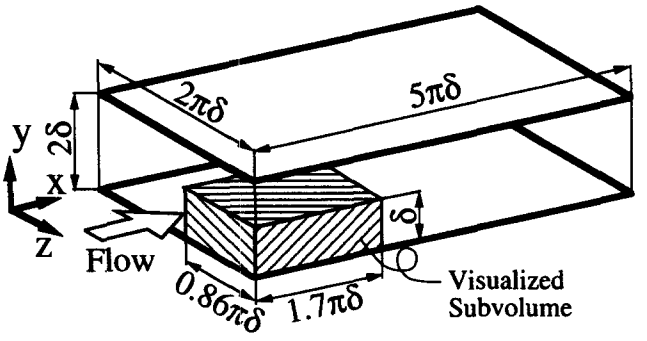

Figure 1 Computational volume, visualized subvolume, and coordinate system

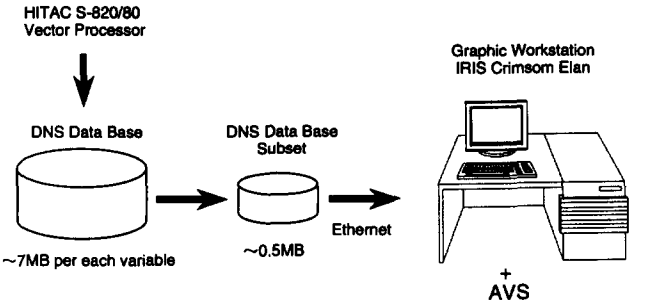

Figure 2 Hardware and data flow for visualization

with those obtained by previous experimental and numerical results (Kuroda et al.; see also Kasagi et al. 1992).

Figure 1 shows the computational domain and the visualized subvolume schematically. The visualized subvolume is $1.7\pi\delta \times \delta \times 0.8\pi\delta$ in the x-, y- and z-directions, which, correspond to about 800, 150, and 400 wall units, respectively. Figure 2 shows the hardware and data flow for visualization. An instantaneous turbulence dataset obtained from the DNS executed on a HITAC S-820/80 supercomputer was divided into 14 data subsets, and one of them was transferred via Ethernet to a graphic workstation (IRIS Crimson Elan). A commercially available 3-D graphics software tool, AVS (Application Visualization System, AVS Inc.), was used for visualization of various turbulence structures.

Results

Detection of near-wall vortical structures

Although vortical structures are believed to play a primary role in turbulent phenomena, widely accepted definition of a vortex does not exist. In this study, the following definition of a vortex proposed by Robinson (1991b) was basically adopted. "A vortex exists when instantaneous streamlines mapped onto a plane normal to the vortex core exhibit a roughly circular or spiral pattern, when viewed from a reference frame moving with the center of the vortex core" (p. 199). However, streamlines are hard to use for automatically detecting 3-D vortical structures even on a high-performance graphics computer. Hence, it is desirable to have a scalar quantity of which a threshold can be used for detection. Robinsion et al. (1990) found that the local low-pressure regions correspond well to the vortex cores. Suzuki and Kasagi (1991) visualized the low-pressure regions in the DNS database of channel flow produced by Kuroda et al. (1994). They also found from examination of associated instantaneous velocity vectors in various cross planes that many of the low-pressure regions were actually created by rotational fluid motions.

In the present study, each of the pressure fluctuation, vorticity, dissipation rate, and the second invariant of the deformation tensor is considered as a candidate indicator of vortical structures, and the distributions of those properties are compared with the instantaneous streamlines.

Low-pressure region. Figure 3(a) shows 3-D contour surfaces of pressure fluctuation, $p'^+ < -3.0$, in a cross-stream (y–z) plane. In this figure, the visualized volume has a dimension of 800 × 150 × 400 (wall units)^3 in the x-, y- and z-directions, respectively, and the grid space is 30 wall units. The lower grid plane corresponds to the bottom wall and the flow direction is from the lower left to the upper right. Instantaneous streamlines and pressure fluctuations in the y–z plane, which is 150 × 400 (wall units)^2, are shown in Figure 3(b). The low-pressure regions; e.g., regions A and B in Figure 3(b), correspond to the cores of vortical fluid motion as reported by Robinson et al. (1990). In Figure 3(b), several additional circular streamlines, where $p'^+ > 0$, can also be seen. This is because the streamlines cannot represent the strength of the vortical fluid motion. It is separately confirmed from the (v'–w') vector diagrams that these vortical motions are very weak. Hence, the low-pressure regions should be interpreted as strong vortical structures. In Figure 3(a), several inclined banana-shaped streamwise vortices can be observed (for the top view, see Figure 14(a)). The diameter and

Notation

p	pressure
Re_θ	Reynolds number based on momentum thickness and maximum velocity
r_{ij}	rotation rate tensor, $(u'_{i,j} - u'_{j,i})/2$
s_{ij}	strain rate tensor, $(u'_{i,j} + u'_{j,i})/2$
u_i	velocity component in the x_i-direction
u, v, w	velocity components in the x-, y- and z-directions
u_τ	friction velocity, $= \sqrt{\tau_w/\rho}$
x, y, z	streamwise, wall-normal, and spanwise coordinates
x_i	ith direction
II	second invariant of deformation tensor, $u_{i,j}u_{j,i}$
II'	fluctuation of the second invariant of deformation tensor, $u'_{i,j}u'_{j,i}$

Greek symbols

δ	channel half width
ε	homogeneous dissipation rate
ν	kinematic viscosity
ρ	density
τ_w	wall shear stress
$\omega_x, \omega_y, \omega_z$	vorticity components in the x-, y- and z-directions

Superscripts and subscripts

$()'$	fluctuating component
$()^+$	normalized by u_τ, ν, and ρ
$\langle\,\rangle$	ensemble average over the x–z plane and time
$()_{,i}$	derivative with respect to x_i

streamwise length of the largest vortex shown here are about 40 and 250 wall units, respectively. When detecting the vortical motions, the the threshold level of pressure, which is presently $p'^+ = -3.0$, is somewhat arbitrarily determined. However, the detection of the vortex core is essentially insensitive to the threshold level; even when it is changed, the vortex core can be detected at the same location, although the diameter and length of the low-pressure region changes accordingly.

Suzuki and Kasagi (1991) classified the vortical structures into four types, i.e.; hairpin-, head-, hook-, and banana-shaped vortices. Among 50 vortical structures they observed, the numbers of inclined banana- and hook-shaped vortices were the largest (21) and the second largest (10), respectively, while the symmetric hairpin-shapes were the rarest (3). Kasagi et al. (1986), Kim et al. (1987), Guezennec et al. (1989), and Robinson et al. (1990) also reported that an asymmetric single vortex is predominant in the near-wall region rather than a pair of counter-rotating vortices. It is noted that two major vortices shown in Figure 3(a) are categorized as banana-shaped vortices, which have been observed most frequently in the present DNS database, as mentioned above.

Robinson (1991b) reported that arch-like vortices are dominant in his visualization. We can conjecture that this discrepancy is owing to the Reynolds number effect. In the present study, the Reynolds number, Re_θ, based on the momentum thickness and the maximum velocity is 229, which is much smaller than that of the database used by Robinson et al. (1990) and Robinson (1991b) ($Re_\theta = 670$). Head and Bandyopadhyay (1981) pointed out some dependency of vortical structures on the Reynolds number, but further investigation is necessary.

Streamwise vorticity and enstrophy. Figure 4(a) shows 3-D contour surfaces of streamwise vorticity, $|\omega'_x| > 0.25$. The instantaneous streamlines and the distribution of streamwise vorticity fluctuation in the same y–z plane as in Figure 3(b) are simultaneously shown in Figure 4(b). The streamwise vorticity is actually large in the vortex core. However, ω'_x is often large at the periphery of a streamwise vortex, and the sign is opposite to that in the vortex core. For instance, the region beneath the vortex exhibits high ω'_x with the opposite sign owing to the nonslip condition at the wall (Kasagi et al. 1986). Additionally, Robinson (1991b) reported that ω'_x is concentrated in local $\partial w'/\partial y$ shear layers. These facts make it difficult to differentiate vortices from shear layers without the streamline and/or vector plots.

Figure 3(a) Three-dimensional (3-D) contour surfaces of pressure fluctuation in the visualized subvolume of 800 × 150 × 400 (wall units)^3: white, $p'^+ < -3.0$

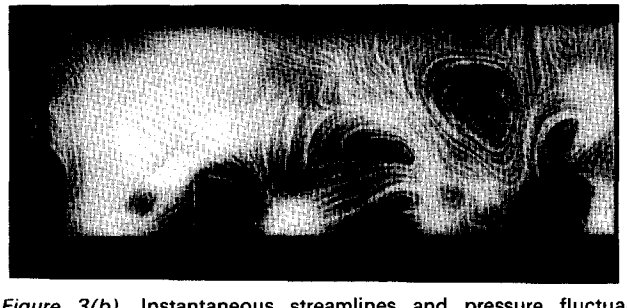

Figure 3(b) Instantaneous streamlines and pressure fluctuation in the y–z plane [150 × 400 (wall units)^2]: gray to black, $p'^+ = 0$ to -3.0; gray to white, $p'^+ = 0$ to $+3.0$

Figure 4(a) 3-D contour surfaces of streamwise voriticity: white, $|\omega'^+_x| > 0.25$

Figure 4(b) Instantaneous streamlines and streamwise vorticity in the y–z plane: gray to white, $\omega'^+_x = 0$ to -0.2; gray to black, $\omega'^+_x = 0$ to $+0.2$

Figure 5(a) shows 3-D contour surfaces of large enstrophy $\omega'_i\omega'_i$, while the instantaneous streamlines and the enstrophy in the y–z plane are shown in Figure 5(b). Among the three components, ω'_z dominates the entrophy in the near-wall region, because the velocity gradient component of $\partial u'/\partial y$ is very large. Therefore, the enstrophy is found to be inappropriate for vortex detection.

Dissipation rate. Figure 6 shows the instantaneous dissipation rate product $s'_{ij}s'_{ij}$ in the y–z plane, where s'_{ij} is defined as follows:

$$s'_{ij} = (u'_{i,j} + u'_{j,i})/2 \tag{1}$$

where a comma followed by an index indicates differentiation with respect to the indexed spatial coordinate. It is noticed that a high dissipation rate exists in any high-shear regions as well as in vortex cores. Thus, the dissipation rate is also inappropriate for vortex detection. Robinson (1991b) reported that the instantaneous dissipation was successfully used for locating vortices in the near-wall region. However, there is an error in his formulation of relating the instantaneous dissipation to the entrophy, which might have produced a mapping with a distinct dissipation peak in the vortex core.

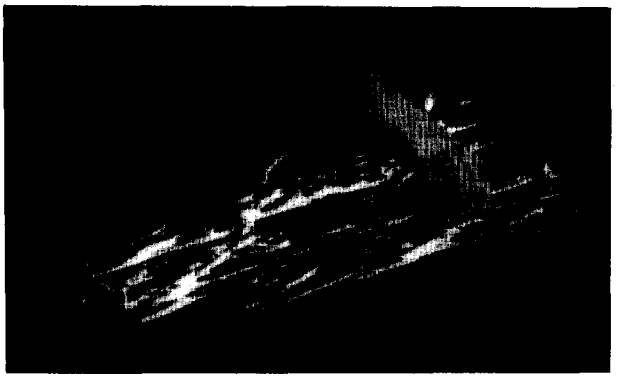

Figure 5(a) 3-D contour surfaces of enstrophy: white, $\omega_i'^+\omega_i'^+ > 0.1$

Figure 5(b) Instantaneous streamlines and enstrophy in the y–z plane: white to black, $\omega_i'^+\omega_i'^+ = 0$ to 0.05

From the above fact, it is interesting to note that the streamwise vortex core is not at the pure solid rotation state, but is under a considerable strain. The distribution of the homogeneous dissipation rate ε $(= \nu u'_{i,j}u'_{i,j})$, which is often used in turbulence modeling, is found similar to that of $s'_{ij}s'_{ij}$, and hence, ε is not an appropriate vortex indicator either (not shown here).

Second invariant of the deformation tensor. The second invariant of the deformation tensor appears in the right-hand side of the Poisson equation of pressure:

$$-p_{,ii}/\rho = u_{i,j}u_{j,i} \equiv II \tag{2}$$

where II can be decomposed as follows:

$$II = 2\bar{u}_{i,j}U'_{j,i} + u'_{i,j}u'_{j,i} + \bar{u}_{i,j}\bar{u}_{j,i} \tag{3}$$

Figures 7(a) and 7(b) show II and the second term on the right-hand side of Equation 3, respectively. From comparison between these figures, the distribution of II and of the second term on the right-hand side of Equation 3 are found almost the same. Hence, the second term on the right-hand side of Equation 3 should be dominant so that the other terms can be neglected. Hereafter, $u'_{i,j}u'_{j,i}$ is denoted as II'. Figure 7(c) shows 3-D contour surfaces of II'. In Figure 7(b), the regions of negative II' correspond to the vortex cores fairly well. Moreover, the regions of positive II' surround the vortex cores. The second invariant of the deformation tensor II' can be written as follows:

$$\begin{aligned} u'_{i,j}u'_{j,i} &= s'_{ij}s'_{ij} - r'_{ij}r'_{ij} \\ &= s'_{ij}s'_{ij} - \omega'_i\omega'_i/2 \end{aligned} \tag{4}$$

where,

$$r'_{ij} = (u'_{i,j} - u'_{j,i})/2 \tag{5}$$

Figure 6 Instantaneous streamlines and dissipation product in the y–z plane: white to black, $s'^+_{ij}s'^+_{ij} = 0$ to 0.02

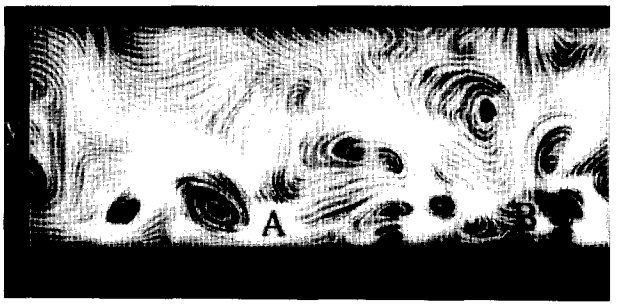

Figure 7(a) Instantaneous streamlines and second invariant of the deformation tensor II in the y–z plane: gray to black, $u^+_{i,j}u^+_{j,i} = 0$ to -0.02; gray to white, $u^+_{i,j}u^+_{j,i} = 0$ to $+0.02$

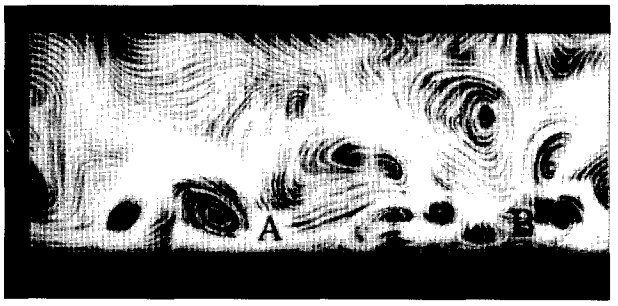

Figure 7(b) Instantaneous streamlines and second invariant of the deformation tensor II' in the y–z plane: gray to black, $u'^+_{i,j}u'^+_{j,i} = 0$ to -0.02; gray to white, $u'^+_{i,j}u'^+_{j,i} = 0$ to $+0.02$

Figure 7(c) 3-D contour surfaces of second invariant of the deformation tensor: white, $u'^+_{i,j}u'^+_{j,i} < -0.02$

From Equation 4, rotation is greater than strain in the regions where $II' < 0$. Because the regions of negative II' correspond to the vortex cores much better than those of high vorticity or dissipation rate alone, it is crucial to take into account relative strength of rotation to strain in the deformation of fluid elements in order to detect near-wall vortices.

Production and destruction of Reynolds stresses in the instantaneous flow field

From the results above, it is clear that low-pressure regions can be interpreted as relatively strong vortical motions. We now discuss their dynamical significance through visualization of various basic processes of turbulence along with the low-pressure regions. Although only a single realization is represented here, most near-wall quasi-streamwise vortices examined are found to play qualitatively similar roles, as discussed in the following.

Figure 8 shows the low-pressure regions and those of large positive Reynolds shear stress product $-u'v'$. The ejection and sweep, which respectively denote outward movement of low-speed fluid and wallward movement of high-speed fluid, exist along both sides of the vortex. Almost all the ejections are associated with the vortical structures, while some of the sweep motions appear without vortices near the wall. The close relationship between the streamwise vortical motion and the high Reynolds shear-stress product is in good qualitative agreement with previous studies (Cantwell 1981; Kasagi et al. 1986, 1992; Lyons et al. 1989; Robinson et al. 1990; Robinson, 1991a, 1991b).

Hereafter, the basic turbulence processes, which are represented by the terms in the transport equations of Reynolds stress, are visualized and examined in detail. We show the spatial relationship between the vortical structure and the modes of fluid motion that should contribute significantly to the averaged budget equations. The budget equation of Reynolds shear stress $-\overline{u'^+v'^+}$ is written as follows:

$$0 = \underbrace{\overline{v'^{+2}}\frac{\partial \bar{u}^+}{\partial y^+}}_{\text{Production}} + \underbrace{\left(\overline{u'^+\frac{\partial p'^+}{\partial y^+}} + \overline{v'^+\frac{\partial p'^+}{\partial x^+}}\right)}_{\text{Velocity pressure-gradient correlation}} + \underbrace{\frac{\partial}{\partial y^+}\overline{u'^+v'^{+2}}}_{\text{Turbulent diffusion}} - \underbrace{\frac{\partial^2}{\partial y^{+2}}\overline{u'^+v'^+}}_{\text{Viscous diffusion}} + \underbrace{2\overline{\frac{\partial u'^+}{\partial x_i^+}\frac{\partial v'^+}{\partial x_i^+}}}_{\text{Dissipation}} \quad (6)$$

Figure 8 3-D contour surfaces of shear product: white, $p'^+ < -3.0$; dark gray, ejection: $(-u'^+v'^+)_2 > 3.0$; light gray, sweep: $(-u'^+v'^+)_4 > 3.0$

where each term has been nondimensionalized by u_τ^4/ν. Note that the velocity pressure-gradient correlation term acts as a major destruction term and almost balances with the production, and that the diffusion terms are relatively small and appreciable only in the region close to the wall (Kasagi et al., 1992; Kuroda et al., 1994; Spalart, 1988).

The instantaneous production of the Reynolds shear stress $v'^{+2}\partial\bar{u}^+/\partial y^+$ in the y–z plane is shown in Figure 9. Regions L and H denote the low- and high-pressure regions, where $p'^+ < -3.0$ and $p'^+ > +3.0$, respectively. It is evident that the stress production distributes quite intermittently in space and takes large values on the both sides of the vortex. A typical pattern of pressure distribution can be seen on the left-hand side in this figure; namely, a large-scale, low-pressure region and two associated high-pressure regions, which are induced by the clockwise rotating vortex. The high-pressure region obliquely above the vortex is formed by the collision of the low-speed fluid ejected with the high-speed fluid convected from upstream, while that on the wall is caused by the impingement of the high-speed fluid onto the wall.

Figure 10 shows the instantaneous velocity pressure-gradient correlation term in the same y–z plane as in Figure 9. From the observation of these terms, Kasagi and Ohtsubo (1993) reported that the production and destruction of the shear stress are vigorous near around the vortex core. This fact is again confirmed in Figures 9 and 10.

The velocity pressure-gradient correlation term can be decomposed into the pressure-strain correlation term and the pressure-diffusion term as follows:

$$u'^+\frac{\partial p'^+}{\partial y^+} + v'^+\frac{\partial p'^+}{\partial x^+} = -p'^+\left(\frac{\partial u'^+}{\partial y^+} + \frac{\partial v'^+}{\partial x^+}\right) + \left(\frac{\partial}{\partial y^+}p'^+u'^+ + \frac{\partial}{\partial x^+}p'^+v'^+\right) \quad (7)$$

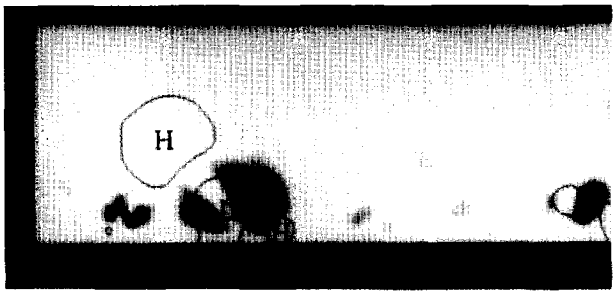

Figure 9 Production for $-\overline{u'v'}$ *in the* y–z plane: white to black, $v'^{+2}(\partial\bar{u}^+/\partial y^+) = 0$ to 0.4

Figure 10 Velocity pressure-gradient correlation for $-\overline{u'v'}$ in the y–z plane: gray to white, $\{u'^+(\partial p'^+/\partial y^+) + v'^+(\partial p'^+/\partial x^+)\} = 0$ to -0.4; gray to black, $\{u'^+(\partial p'^+/\partial y^+) + v'^+(\partial p'^+/\partial x^+)\} = 0$ to $+0.4$

Figure 11 Pressure-strain for $-\overline{u'v'}$ in the y–z plane: gray to white, $-p'^{+}\{(\partial u'^{+}/\partial y^{+}) + (\partial v'^{+}/\partial x^{+})\} = 0$ to -0.4; gray to black, $-p'^{+}\{(\partial u'^{+}/\partial y^{+}) + (\partial v'^{-}/\partial x^{+})\} = 0$ to $+0.4$

Figure 12 Pressure diffusion for $-\overline{u'v'}$ *in the* y–z plane: gray to white, $\partial(p'^{+}u'^{+})/\partial y^{+} + \partial(p'^{+}v'^{+})/\partial x^{+} = 0$ to -0.4; gray to black, $\partial(p'^{+}u'^{+})/\partial y^{+} + \partial(p'^{+}v'^{+})/\partial x^{+} = 0$ to 0.4

Hence, instantaneous distributions of these terms together with the low-pressure regions in the y–z plane are shown in Figures 11 and 12. The high pressure-strain regions, which are known to act as a dominant sink in the Reynolds shear stress budget, exist in both high- and low-pressure regions. In Figure 12, the negative pressure-diffusion regions, where $-\overline{u'v'}$ is lost, exist in between the high- and low-pressure regions. In contrast, the positive diffusion regions, where $-\overline{u'v'}$ is gained, exist inside the high- and low-pressure regions. Although the pressure diffusion is negligibly small compared with the pressure-strain correlation in the averaged budget of the Reynolds shear stress, the former is on the same magnitude as the latter in the instantaneous flow field.

The instantaneous turbulent diffusion term $\{\partial(u'^{+2}v'^{+})/\partial x^{+} + \partial(u'^{+}v'^{+2})/\partial y^{+} + \partial(u'^{+}v'^{+}w'^{+})/\partial z^{+}\}$ in the y–z plane is shown in Figure 13. It is noted that only y-derivative term survives when the averaged Reynolds stress equation, i.e., Equation 6, is derived. The negative turbulent diffusion region exist on the both sides of the vortex, where the production is large. The positive turbulent diffusion regions exist in the regions between the high- and low-pressure regions. As a result, the turbulent diffusion transports $-\overline{u'v'}$ from the production regions to the regions between high- and low-pressure regions. Thus, these diffusion terms cannot be neglected in an analysis of the kinematics of the near-wall turbulence structures. On the other hand, the viscous diffusion and the dissipation rate terms were found to be negligible in the instantaneous field as well as in the averaged budget of the Reynolds shear stress (not shown here).

Figure 14(b) shows the distribution of spanwise vorticity ω'_z in the x–y cross section shown in Figure 14(a). An internal shear layer is clearly observed as negative regions of spanwise vorticity fluctuation. As Robinson et al. (1990) reported, the internal shear layer is elongated in the streamwise direction, accompanied by a local stagnation region, where $p' > 0$. They also found that the internal shear layer often rolls up into a transverse vortex element and pointed out some dynamical importance of the transverse vortices. In the present database, there exists only an inclined streamwise vortex as mentioned above, so that ω'_z does not show marked peak at the tip of the shear layer and the roll-up into a low-pressure region is rather weak. It is noted that the streamwise vortex has a tilt to the spanwise direction, as can be seen in Figure 14(a). Thus, it is conjectured that, instead of the transverse vortex element, the tilt of the streamwise vortex contributes to this weak roll-up.

The spatial relationship between the near-wall quasi-streamwise vortex and the production, destruction, and diffusion of $-\overline{u'v'}$ is schematically illustrated in Figure 15. A low-pressure region corresponds to the core of an inclined streamwise vortex near the wall. On the sweep side of the vortex, the

Figure 13 Turbulent diffusion for $-\overline{u'v'}$ *in the* y–z plane: gray to white, $\partial(u'^{+2}v'^{+})/\partial x^{+} + \partial(u'^{+}v'^{+2})/\partial y^{+} + \partial(u'^{+}v'^{+}w'^{+})/\partial z^{+} = 0$ to -0.4; gray to black, $\partial(u'^{+2}v'^{+})/\partial x^{+} + \partial(u'^{+}v'^{+2})/\partial y^{+} + \partial(u'^{+}v'^{+}w'^{+})/\partial z^{+} = 0$ to $+0.4$

Figure 14(a) Spanwise vorticity ω'_z *in the* x–z plane: gray to black, $\omega'^{+}_z = 0$ to -0.2; gray to white, $\omega'^{+}_z = 0$ to $+0.2$; white, $p'^{+} < -3.0$

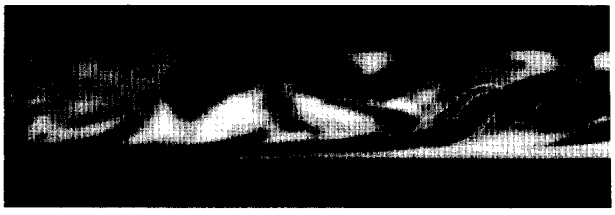

Figure 14(b) Spanwise vorticity ω'_z in the x–y plane: gray to black, $\omega'^{+}_z = 0$ to -0.2; gray to white, $\omega'^{+}_z = 0$ to $+0.2$; lines, $p'^{+} = -3.0, -4.0, -4.7, +3.0, +4.2, +5.5$

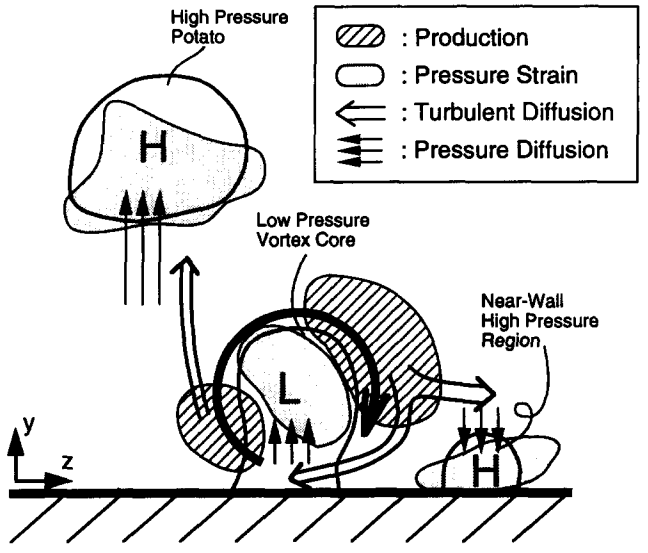

Figure 15 Relationship between a near-wall quasi-streamwise vortex and the production, pressure-strain, and diffusion of $-\overline{u'v'}$

Figure 16 Production for $\overline{u'^2}$ in the y–z plane: gray to black, $-2u'^+v'^+(\partial\bar{u}^+/\partial y^+) = 0$ to -0.4; gray to white, $-2u'^+v'^+(\partial\bar{u}^+/\partial y^+) = 0$ to $+0.4$

high-pressure region near the wall is produced by the fluid impingement onto the wall that is induced by the vortex motion. On the ejection side of the vortex, low-speed fluid is lifted up, and its collision against high-speed fluid from upstream forms a local stagnation region, where $p' > 0$. Instantaneous high production rate of the Reynolds shear stress takes place on both sides of the vortex. The low- and high-pressure regions are regarded as high destruction (pressure-strain correlation) regions of the Reynolds stress. The turbulent diffusion transports the Reynolds shear stress from the high production regions to the regions between the high- and low-pressure regions. The pressure diffusion further transports the Reynolds stress from the regions between the high- and low-pressure regions to the high destruction regions.

The budget equations of normal stresses are derived as follows:

$$0 = -2\overline{u'^+v'^+}\frac{\partial\bar{u}^+}{\partial y^+} + 2\overline{p'^+\frac{\partial u'^+}{\partial x^+}} - \frac{\partial}{\partial y^+}\overline{u'^{+2}v'^+} + \frac{\partial^2}{\partial y^{+2}}\overline{u'^{+2}} \quad 0 \quad -2\overline{\frac{\partial u'^+}{\partial x_i^+}\frac{\partial u'^+}{\partial x_i^+}} \tag{8}$$

$$0 = \quad 0 \quad + 2\overline{p'^+\frac{\partial v'^+}{\partial y^+}} - \frac{\partial}{\partial y^+}\overline{v'^{+3}} + \frac{\partial^2}{\partial y^{+2}}\overline{v'^{+2}} - 2\frac{\partial}{\partial y^+}\overline{p'^+v'^+} - 2\overline{\frac{\partial v'^+}{\partial x_i^+}\frac{\partial v'^+}{\partial x_i^+}} \tag{9}$$

$$0 = \quad 0 \quad + 2\overline{p'^+\frac{\partial w'^+}{\partial z^+}} - \frac{\partial}{\partial y^+}\overline{v'^{+2}w'^{+2}} + \frac{\partial^2}{\partial y^{+2}}\overline{w'^{+2}} \quad 0 \quad -2\overline{\frac{\partial w'^+}{\partial x_i^+}\frac{\partial w'^+}{\partial x_i^+}} \tag{10}$$

Production | Pressure-strain correlation | Turbulent diffusion | Viscous diffusion | Pressure diffusion | Dissipation

Figure 17 Pressure-strain for $\overline{u'^2}$ in the y–z plane: gray to black, $2p'^+(\partial u'^+/\partial x^+) = 0$ to -0.4; gray to white, $2p'^+(\partial u'^+/\partial x^+) = 0$ to $+0.4$

Figure 18 Pressure-strain for $\overline{v'^2}$ in the y–z plane: gray to black, $2p'^+(\partial v'^+/\partial y^+) = 0$ to -0.4; gray to white, $2p'^+(\partial v'^+/\partial y^+) = 0$ to $+0.4$

The production of the Reynolds normal stress $\overline{u'^2}$ in the same y–z plane is shown in Figure 16. The large production of $\overline{u'^2}$ takes place on the both sides of the vortex like that of the shear stress. This is in accordance with Lyons et al. (1989).

The redistributions of the Reynolds normal stresses $\overline{u'^2}$, $\overline{v'^2}$, and $\overline{w'^2}$ through the pressure-strain correlation in the same y–z plane are shown in Figures 17, 18, and 19, respectively. In Figure 17, the pressure-strain correlation term for $\overline{u'^2}$; i.e., $2'(\partial u'/\partial x)$ is shown. In almost the whole field, this term is negative, and the turbulent kinetic energy is redistributed from the u-component to the others. Especially in the vortex core and in the two associated high-pressure regions, the loss is quite large, so that the redistribution is even more vigorous. In Figure 18, the pressure-strain correlation term for $\overline{v'^2}$ is shown. It is found that this term is positive in the vortex core and negative around it. In the core of the high-pressure region away from the wall, $2p'(\partial v'/\partial y)$ is positive, while it is negative in the lower part of this region as well as in the high-pressure region attached to the wall.

The pressure-strain correlation term for $\overline{w'^2}$ is shown in Figure 19. It is negative in the low-pressure vortex core and positive around it. On the other hand, in the two high-pressure regions, the pressure-strain is positive so that $\overline{w'^2}$ is gained.

In summary, the core of the vortex, the redistribution from $\overline{u'^2}$ and $\overline{w'^2}$ to $\overline{v'^2}$ occurs, while that from $\overline{v'^2}$ to $\overline{w'^2}$ occurs around the vortex. In the high-pressure region away from the wall, turbulent kinetic energy is transferred from $\overline{u'^2}$ to $\overline{v'^2}$ and $\overline{w'^2}$. This is because the low-speed fluid ejected by the vortical motion collides with the high-speed ($u' > 0$) fluid convected from upstream, and then the high-speed fluid changes its flowing direction to the y- or z-direction. In the lower part of the high-pressure region away from the wall, the redistribution from $\overline{v'^2}$ to $\overline{u'^2}$ and $\overline{w'^2}$ occurs. In the high-pressure region near the wall, the redistribution from $\overline{u'^2}$ and $\overline{v'^2}$ to $\overline{w'^2}$ occurs. This is because the sweep motion induced by the vortex gives rise to the "splatting" on the wall (see, e.g., Lee and Hunt 1988; Moin and Kim 1982).

Helicity

The 3-D contour surfaces of helicity and of low- and high-speed streaks are shown in Figures 20 and 21, respectively. The helicity is defined as $u_i'\omega_i'$, and the streaks are presently distinguished as the regions of $|u'^+| > 4.0$. A strong resemblance can be observed between the distributions of helicity and streaks, and thus, the streaky structures elongated in the streamwise direction should carry most of the helicity in the near-wall region. It is known that the energy cascade should be suppressed when the helicity takes a large value (Yoshizawa and Yokoi, 1992), so relatively long persistence of the streaky structures is related to this close correspondence between the high-helicity regions and the streaky structures.

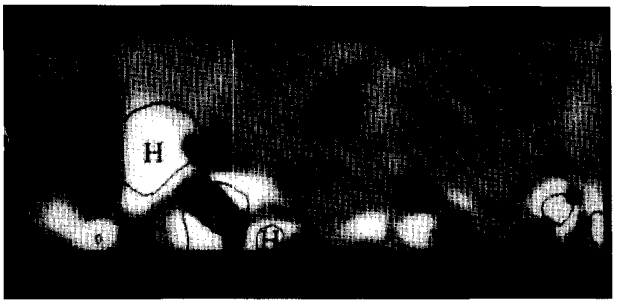

Figure 19 Pressure-strain for $\overline{w'^2}$ in the y–z plane: gray to black, $2p'^+(\partial w'^+/\partial z'^+) = 0$ to -0.4; gray to white, $2p'^+(\partial w'^+/\partial z'^+) = 0$ to $+0.4$

Figure 20 3-D contour surfaces of helicity and pressure fluctuation: white, $p'^+ < -3.0$; gray, $|u_i'^+\omega_i'^+| > 0.6$

Figure 21 3-D contour surfaces of streamwise velocity and pressure fluctuation: white, $p'^+ < -3.0$; gray, $|u'^+| > 4.0$

Conclusions

The near-wall quasi-coherent turbulence structures in a DNS database of turbulent channel flow were investigated by using a 3-D computer graphics technique. The following conclusions are derived.

(1) Both the low-pressure regions and those of negative second invariant of the deformation tensor correspond to the cores of vortical motion fairly well. The latter indicates the local region where the rotation of a fluid element excels the strain in strength. Hence, even weak vortical motions can be detected by the negative second invariant of the deformation tensor, while only strong ones can be marked by the low-pressure regions.

(2) The near-wall, quasi-streamwise vortical structures play a primary role in the production and destruction of the Reynolds shear stress. Under a characteristic phase relationship, the production, pressure-strain, pressure diffusion, and turbulent diffusion mechanisms are distributed closely around the vortical structure.

(3) The production and redistribution of the Reynolds normal stresses are also dominated by the streamwise vortical structures; the high $\overline{u'^2}$ production regions exist on both sides of the vortices, while the redistribution to other components occurs inside the low- and high-pressure regions associated with the vortical structure. Thus, the occurrence of the essential mechanism of near-wall turbulence is highly intermittent in space and is concentrated in the region of the inclined streamwise vortical structure.

(4) The high-helicity regions are elongated in the streamwise direction and are mostly associated with the streaky structures.

References

Cantwell, B. J. 1981. Organized motion in turbulent flows. *Annu. Rev. Fluid Mech.*, J. L. Lumley, M. Van Dyke and H. L. Reed, (eds.), **13**, 457–515

Guezennec, Y. G., Piomelli, U. and Kim, J. 1989. On the shape and dynamics of wall structures in turbulent channel flow. *Phys. Fluids: A*, **1**, 764–766

Head, M. R. and Bandyopadhyay, P. 1981. New aspects of turbulent boundary layer structure. *J. Fluid Mech.*, **107**, 297–338

Kasagi, N., Hirata, M. and Nishino, K. 1986. Streamwise pseudo-vortical structure and associated vorticity in the near-wall region of a wall-bounded turbulent shear flow. *Exp. Fluids*, **4**, 309–318

Kasagi, N., Tomita, Y. and Kuroda, A. 1992. Direct numerical simulation of passive scalar field in a two-dimensional turbulent channel flow. *J. Heat Transfer*, **114**, 598–606

Kasagi, N. and Ohtsubo, Y. 1993. Direct numerical simulation of low Prandtl number thermal field in a turbulent channel flow. *Turbulent Shear Flows VIII*, F. Durst, R. Friedrich, B. E. Launder, F. W. Schmidt, U. Schumann and J. H. Whitelaw, (eds.). Springer, Berlin, 97–119

Kim, H. T., Kline, S. J. and Reynolds, W. C. 1971. The production of turbulence near a smooth wall in a turbulent boundary layer. *J. Fluid Mech.*, **50**, 133–160

Kim, J., Moin, P. and Moser, R. 1987. Turbulent statistics in fully developed channel flow at low Reynolds number. *J. Fluid Mech.*, **177**, 133–166

Kline, S. J., Reynolds, W. C., Schraub, F. A. and Runstadler, P. W. 1967. The structure of turbulent boundary layers. *J. Fluid Mech.*, **30**, 741–773

Kuroda, A., Kasagi, N. and Hirata, M. 1994. Direct numerical simulation of turbulent plane Couette-Poiseuille flows: Effect of mean shear rate on the near-wall turbulence structures. *Turbulent Shear Flows IX*, F. Durst, N. Kasagi, B. E. Launder, F. W. Schmidt, K. Suzuki and J. H. Whitelaw, (eds.). Springer, Berlin, in press

Lee. M. J. and Hunt, J. C. R. 1988. The structure of sheared turbulence near a plane boundary. *Proc. CTR Summer Program*, Center for Turbulence Research, Stanford University, Stanford, CA, 221–241

Lyons, S. L., Hanratty, T. J. and McLaughlin, J. B. 1989. Turbulence-producing eddies in the viscous wall region. *AIChE.J.*, **35**, 1962–1974

Moin, P. and Kim, J. 1982. Numerical investigation of turbulent channel flow. *J. Fluid Mech.*, **118**, 341–377

Robinson, S. K., Kline, S. J. and Spalart, P. R. 1990. Quasi-coherent structures in the turbulent boundary layer: Part II, verification and new information from a numerically simulated flat-plate layer. *Near Wall Turbulence*, S. J. Kline and N. H. Afgan, (eds.). Hemisphere, Washington, DC, 218–247

Robinson, S. K. 1991a. Coherent motions in the turbulent boundary layer. *Annu. Rev. Fluid Mech.*, J. L. Lumley, M. Van Dyke, and H. L. Reed, (eds.), **23**, 601–639

Robinson, S. K. 1991b. The kinematics of turbulent boundary layer structure. NASA TM-103859

Spalart, P. R. 1988. Direct simulation of a turbulent boundary layer up to $Re_\theta = 1410$. *J. Fluid Mech.*, **187**, 61–98

Suzuki, Y. and Kasagi, N. 1991. Temporal evolution of the coherent structures in a turbulent flow (in Japanese). *Proc. 69th JSME Fall Annual Meeting*, **B**, 233–235

Yoshizawa, A. and Yokoi, N. 1992. Coherent structures in turbulence and their relationship with the breakage of spatial symmetry. *J. Inst. Ind. Sci.*, University of Tokyo, **44**, 50–55